POLITECNICO MILANO 1863

SCUOLA DI INGEGNERIA INDUSTRIALE E DELL'INFORMAZIONE

EXECUTIVE SUMMARY OF THE THESIS

Evaluation of Silicon Carbide for Integrated Photonics

LAUREA MAGISTRALE IN TELECOMMUNICATION ENGINEERING - INGEGNERIA DELLE TELECOMUNICAZIONI

Author: MEHMET NURETTIN GEÇKİL

Advisor: PROF. ANDREA MELLONI

Co-advisor: ANDRÉS MARTÍNEZ PHD.

Academic year: 2025-26

1. Introduction

Integrated photonics enable compact on-chip quantum and classical optical signal processing. silicon is the dominant material platform due to its mature fabrication ecosystem; however, its 1.12 eV bandgap leads to two-photon and free-carrier absorption at 1550 nm, limiting high-power nonlinear performance. This has motivated the development of wide-bandgap alternatives such as Si_3N_4, AlN, $LiNbO_3$, III–V semiconductors, and SiC.

SiC is a mature material widely used in power electronics and mechanical applications. It offers high thermal conductivity ($3.7\ \mathrm{W\,cm^{-1}\,K^{-1}}$), a wide bandgap (3.2 eV) and transparency window (VIS to NIR), and compatibility with wafer-scale processing [1]. The development of 4H-SiC-on-insulator (4H-SiCOI) substrates enables strong refractive-index contrast and has demonstrated micro-ring resonators with quality factors exceeding 10^6[2] thanks to its higher crystal quality in contrast to its other polytypes.

Although Si ($n = 3.47$) provides stronger confinement than 4H-SiC ($n \approx 2.6$), 4H-SiC suppresses two-photon absorption at telecom wavelengths and supports intrinsic second-order nonlinear and electro-optic effects absent in Si, together with improved thermal stability. These characteristics motivate a focused evaluation of the 4H-SiCOI platform for integrated photonics. This thesis investigates the design and fabrication of strongly confined 4H-SiCOI waveguides for integrated photonic applications. Numerical simulations were performed to analyze the modal confinement and bending performance of buried-strip waveguides. Also, the optimization of the lithography and etching processes for the waveguide fabrication was done. The study concludes with an evaluation of the platform and perspectives for future 4H-SiCOI photonic devices.

2. Waveguide Design Scheme

The modeled structure consisted of a 4H-SiC core embedded in SiO_2 with 85° sidewalls (see Fig. 1) to reflect fabrication constraints [1]. Parametric sweeps were performed using the Lumerical MODE FDE solver at 1550 nm, with the waveguide height varied between 100-1250 nm and the width between 200-1250 nm, each sampled at 30 points. These limits follow literature-reported dimensions while also enabling exploration of smaller waveguide geometries that may be achievable in practice. Convergence tests ensured stability of the effective index up to the third decimal place, and fixed mesh and window settings were maintained to guarantee numerical consistency.

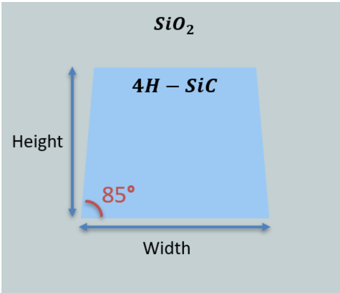

Figure 1: Cross section

For each geometry, the five modes with the highest effective refractive indices were computed to identify fundamental and higher-order TE and TM modes and to construct design maps describing modal confinement and single- to multi-mode transitions. For each mode, the extracted parameters included field distributions, effective refractive index, group index, effective mode area, TE polarization fraction, and propagation loss.

To preserve physical continuity across parameter sweeps, a mode-tracking algorithm was implemented in MATLAB App Designer. Since the solver orders modes by descending n_{eff} independently of TE fraction, tracking was performed sequentially by initializing modes at the first sweep point and matching subsequent solutions based on monotonic evolution. When TE-fraction values were clearly separated, matching minimized TE-fraction variation; near degeneracy, it minimized variations in the slope of n_{eff} with respect to the swept dimension. Waveguides were modeled as lossless and anisotropic at 1550 nm using ellipsometrically extracted indices. Modal quantities were computed on a discrete grid and interpolated in MATLAB to generate smooth design maps.

2.1. Single-Mode Waveguide Designs

The study defines admissible rectangular 4H–SiCOI waveguide geometries over a range of aspect ratios. For each AR, the largest cross-section preserving single-TE operation is denoted as Maximum Confinement–Single TE (MC–STE), while the corresponding single-TM case is defined as Maximum Confinement–Single TM (MC–STM), representing the largest geometries within the single-mode regime. The mode-labeling convention follows the framework of [3]. TE_{11} and TM_{11} denote the fundamental modes, while TE_{21} and TM_{21} denote the first higher-order modes. For AR > 1 (AR = Width/Height), the single-mode cutoff in MC-STE designs is determined by TE_{21}, whereas in MC-STM designs it is determined by TM_{21}; for AR < 1, the corresponding cutoff modes are their 90°-rotated counterparts, ensuring continuous cutoff boundaries across the geometrical space.

Tracking the modes via TE-fraction reveals the expected TE/TM interchange near AR = 1 (the case for Si [3]), but in 4H-SiCOI the transition occurs around AR $\approx$ 1.08. This shift is mainly attributed to the birefringence of 4H-SiC, where the vertical c-axis possesses a slightly higher refractive index in the vertical direction, displacing the symmetry point toward larger AR values. Figure 2 shows the MC-STE and MC-STM () contours over a broad AR range, each defining the boundary for single-mode operation. The results indicate that TE waveguides must become progressively thinner ($\sim$100 nm) to remain single-mode, whereas wide TM geometries can sustain single-mode behavior even above 200 nm thickness.

2.2. Mode effective and group indices

The variation of n_{eff} and n_{g} with AR provides direct insight into modal confinement and resonator-level performance. Fig.s 3 and 4 show the n_{eff} and n_{g} of the MC-STE and MC-STM design families as functions of AR, with emphasis on the TE_{11} mode in MC-STE and the TM_{11} mode in MC-STM. The n_{eff} serves as a measure of confinement, while the group index n_{g} governs resonator metrics such as free spectral range (FSR) and quality factor Q, with larger n_{g} leading to reduced FSR and increased Q for fixed geometry and distributed loss.

In the MC-STE configuration, maximum TE_{11} confinement occurs near AR $\approx$ 1.62 (approximately 595 $\times$ 367 nm), while the corresponding TM_{11} maximum appears near AR $\approx$ 0.61. For AR < 0.2, the TE_{11} effective index approaches the cladding index, indicating weak confinement and excluding this region for TE designs. The index curves exhibit approximate symmetry around AR $\approx$ 1.08, reflecting the equivalence of width–height interchange and the correspondence between TE and TM configurations. In the MC-STM family, strongest TM_{11} confinement is obtained near AR $\approx$ 0.66 (approximately 440×660 nm), while TE_{21} becomes degenerate with TM_{11} near AR $\approx$ 4, increasing susceptibility to TE–TM coupling and making operation near this region undesirable.

Considering these trends, a representative TE geometry of width of 700 nm and height of 300 nm was selected (AR $\approx$ 2.33). Although maximum TE confinement would yield $n_{\text{eff,TE}} \approx$ 1.93, the TM mode remains strongly guided at that point ($n_{\text{eff,TM}} \approx$ 1.80). The chosen compromise geometry maintains strong TE confinement ($n_{\text{eff,TE}} \approx$ 1.90) while reducing TM confinement ($n_{\text{eff,TM}} \approx$ 1.66), remaining consistent with conventional 2:1 TE waveguide design practice. Since the maps rely on interpolation and curve fitting, the objective was not strict optimization but identification of practically usable dimensions to initiate fabrication.

3. Waveguide Bending Analysis

Realization of integrated photonic devices on the 4H-SiCOI platform requires evaluation of bent waveguides in addition to straight sections, particularly for ring resonator applications. Bending-radius sweeps were performed for selected geometries extracted from the design maps, and angular losses were analyzed. In regimes where extremely low losses are expected, negative values were occasionally obtained due to numerical instabilities associated with PML boundary reflections.

Brute-force tuning of PML parameters and FDE window settings in Lumerical MODE did not yield a globally stable solution across all geometries and radii. Therefore, bent-waveguide simulations were implemented in Tidy3D, where numerical instability was mitigated by enlarging the computational domain to increase separation from the PML boundaries. An automated radius-sweep algorithm adaptively adjusted the domain size only when required, ensuring physically consistent positive angular loss values while controlling computational cost.

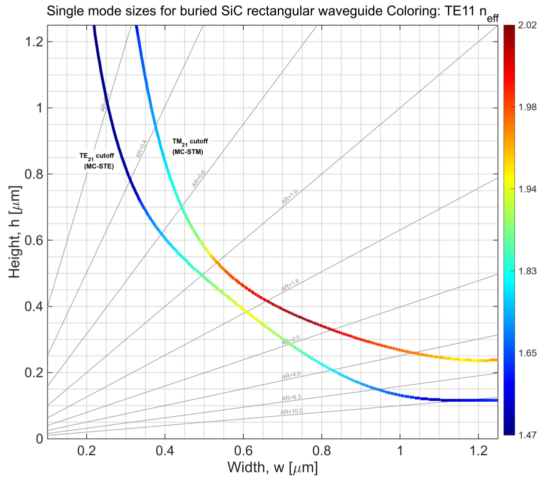

Figure 2: Map of Maximally Confined Single-Mode 4H-SiCOI Waveguide Cross-sections

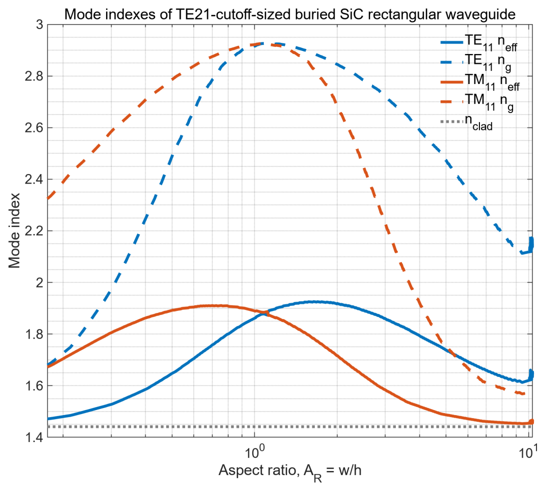

Figure 3: Mode Indexes of the TE_{21} Cutoff-Sized 4H-SiCOI Rectangular Waveguide

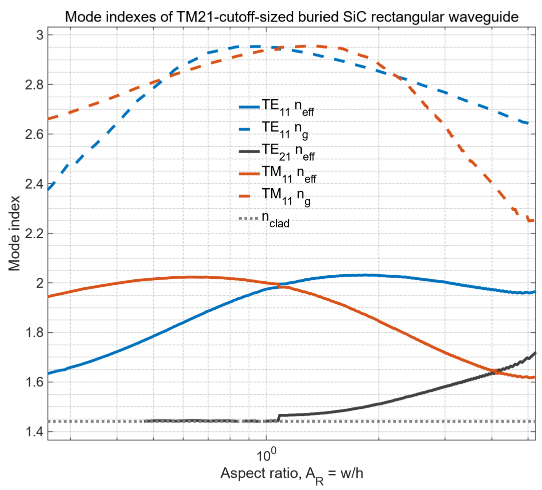

Figure 4: Mode Indexes of the TM_{21} Cutoff-Sized 4H-SiCOI Rectangular Waveguide

In Tidy3D bent-waveguide simulations, additional modes were computed, radiation-like solutions were filtered by confinement, and the highest-index confined mode was used to construct bending-performance maps. Default PML layers and 15 points-per-wavelength resolution at 1550 nm were used, together with adaptive FDE domain sizing. Selected MC-STE and MC-STM design sized ring resonator usage was simulated over varying bend radii and the results were parabolically fitted. The minimum bending radius required to sustain a radiation-limited quality factor $Q = 2.5 \times 10^6$ was extracted using

$$Q \approx \frac{40\pi^2 R\, n_g}{\lambda_0 \ln 10\, L_{\mathrm{dB90}}} = \frac{0.2\,\pi\, n_g}{\lambda_0 \ln 10\, L_{\mathrm{dB/cm}}}, \qquad (1)$$

where R is the bend radius and L_{dB90} the angular loss. Both TE and TM fundamental modes support small radii at high Q, but the TM mode allows smaller radii due to stronger vertical confinement enhanced by 4H-SiC birefringence, although tall narrow geometries remain more fabrication-sensitive.
Using the extracted radii and group indices, the maximum FSR was evaluated from

$$\mathrm{FSR} = \frac{c_0}{n_g L} = \frac{c_0}{2\pi n_g R}, \qquad (2)$$

with $L = 2\pi R$. High-Q resonators (2.5×10^5–2.5×10^6) can achieve FSR values on the order of 1 THz or higher for the proposed single mode geometries (Fig. 5 and Fig. 6). Although the target Q varies by an order of magnitude, the overall trends of the bending-radius and FSR maps remain largely unchanged.

3.1. Bending Results for the Proposed Waveguide

The selected pilot waveguide geometry of 700 nm×300 nm was analyzed using adaptive radius sweep method to evaluate its suitability for ring-resonator implementations. At the corresponding AR (AR ≈ 2.33), bending simulations confirmed that only the fundamental TE mode remains guided (see Fig. 5 and Fig. 6), while the TM mode is cut off. Utilizing calculated propagation losses in $\alpha_{\mathrm{ang}} = R\,\alpha_{\mathrm{prop}}$, the angular losses of the TE mode are shown in Fig. 7a.

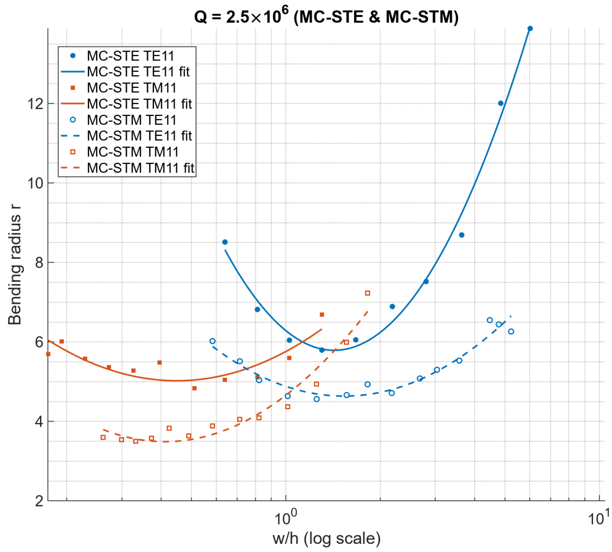

Figure 5: Minimum bending radius required to achieve a radiation-limited quality factor $Q = 2.5 \times 10^6$ for MC-STE and MC-STM designs. Even if the target Q changes by an order of magnitude, the overall trend remains essentially unchanged.

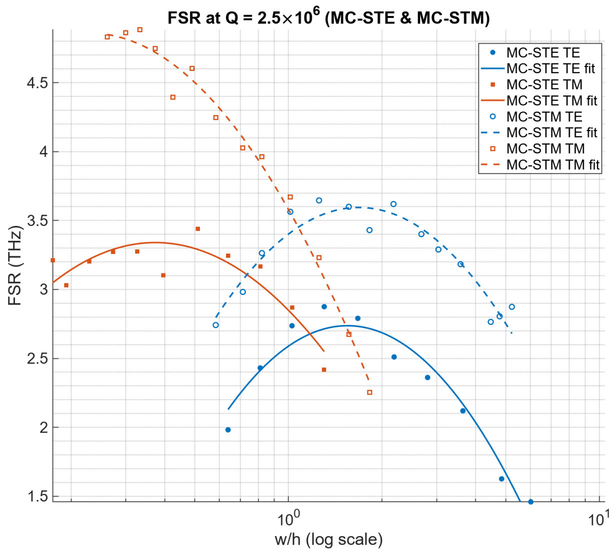

Figure 6: Maximum FSR values corresponding to $Q = 2.5 \times 10^6$ for MC-STE and MC-STM designs. The stronger confinement of the fundamental TM mode is consistently reflected in these results.

They are minimized for bending radiuses over 6 μm. Using Eqs. 1 and 2, the achievable quality factor and corresponding free spectral range (FSR) were computed as functions of bending radius. For $\lambda_0 = 1550$ nm, a target $Q = 2.5 \times 10^5$ requires $R = 5.0736$ μm, yielding FSR =

3.4156 THz, while $Q = 2.5 \times 10^6$ requires $R = 6.4764$ μm with FSR = 2.6713 THz (Fig. 7b-7c).The discrepancies observed at 8.5 μm and 10 μm in Fig. 7a arise from solver-related errors when evaluating extremely low propagation losses (on the order of 10^{-9}). For bending radii beyond 10.5 μm, the solver returns zero propagation loss due to the lossless material model, resulting in an infinite calculated Q.

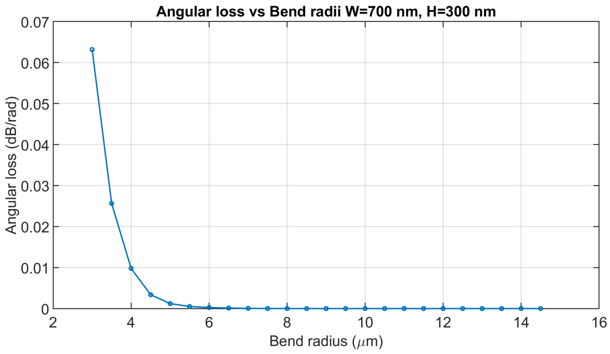

(a) Angular Loss vs Bend radii

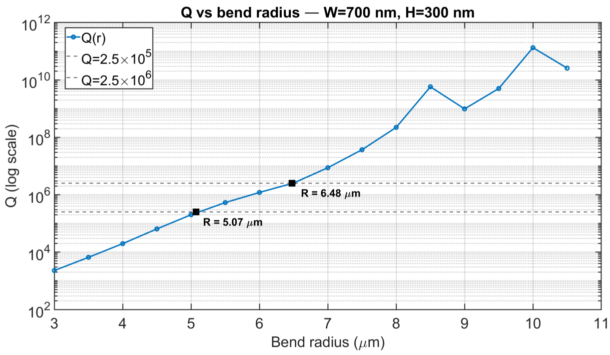

(b) Q vs Bend radii

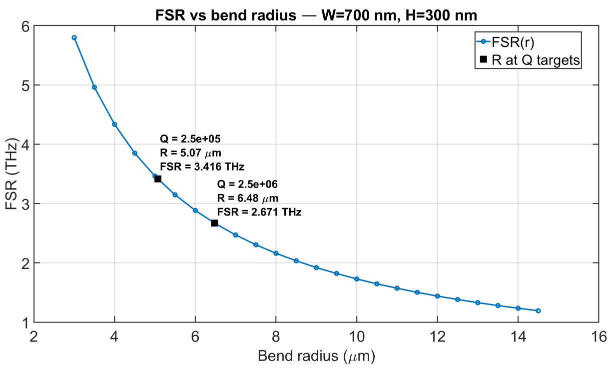

(c) FSR vs Bend radii

Figure 7: Angular loss, quality factor and FSR for 700×300 nm^2 bent waveguide.

4. SiC/SiCOI Characterization

Although SiC is well established in electronics, its integration into optical fabrication required adaptation of cleanroom processes at PoliFAB. To reduce material risk and cost, lithography and etching were first developed on a 4-inch HPSI bulk 4H-SiC wafer (diced to $15 \times 15\,\text{mm}^2$) and subsequently transferred to $20 \times 20\,\text{mm}^2$ HPSI 4H-SiCOI samples.

Spectroscopic ellipsometry was performed on bulk and thin-film samples to extract the ordinary and extraordinary refractive indices. Both show normal dispersion and agree with reference data at 1550 nm. The thin film exhibits a slightly lower index, attributed to fabrication effects, but the deviation remains small. Due to color variations on the SiCOI samples, two independent measurements were fitted with the same model and yielded consistent results. The extinction coefficient at 1550 nm was effectively zero for both samples, consistent with the simulation assumptions.

Despite slight refractive-index reduction in the thin film and observed surface color variations, repeated measurements and model fitting showed strong agreement. The extinction coefficient at 1550 nm was determined to be effectively zero for both sample types, consistent with simulation assumptions.

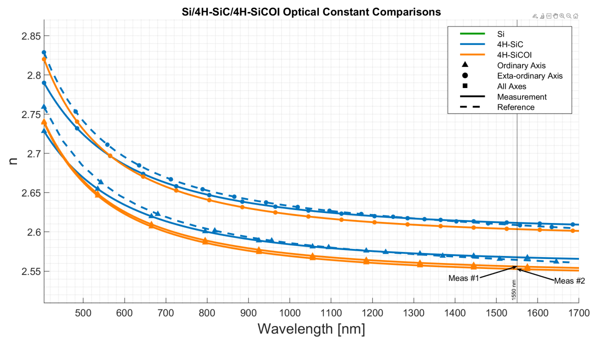

Figure 8: Measured n compared with literature [4]; solid lines are measurements, dashed lines reference data. Triangles are $n(o)$ and circles are $n(e)$.

Sample	$n(o)$	$n(e)$
4H-SiC	2.567	2.611
4H-SiCOI #1	2.555	2.603
4H-SiCOI #2	2.552	2.603
4H-SiC [4]	2.564	2.608

Table 1: Refractive index values at $\lambda = 1550$ nm.

5. Waveguide Fabrication

5.1. Lithography

Lithography was performed on bulk 4H-SiC using the MLA100 (365 nm i-line) with AZ® 15nXT negative photoresist. Line–space patterns from 1 to 10 μm were evaluated, targeting reliable 1 μm linewidth and spacing at the tool's resolution limit to enable transition to submicron EBL patterning. Dose and mask-dimension combinations were calibrated for all geometries, including resolution-limit structures. Optimized parameters were a dose of 110 and a defocus of -1, where a 750 nm mask line produced a 1 μm feature and a 1.25 μm mask gap yielded a 1 μm spacing.

Non-uniform resist profiles require compensation between dose and mask dimensions to mitigate proximity effects. The high transparency of 4H-SiC at 365 nm reduces surface reflections and complicates polymerization control, making the 1 μm line–space case the most challenging; larger geometries yielded more stable profiles with reduced taper.

5.2. Etching

Reactive ion etching was performed using the SPTS Omega SYNAPSE 200 LPX module with SF_6 (100 sccm) and O_2 (10 sccm) at 10 mTorr, 1500 W ICP power, 200 W CCP bias power, and a platen temperature of -10°C. Under these conditions, the etch rate of bulk 4H–SiC was 0.575 μm/min ($\pm$0.013 μm/min), while the AZ® 15nXT photoresist mask exhibited an etch rate of 1.44 μm/min ($\pm$0.06 μm/min). The resulting etch selectivity is therefore $S_{\mathrm{SiC:PR}} = R_{\mathrm{SiC}}/R_{\mathrm{PR}} = 0.575/1.44 \approx 0.40 \pm 0.02$.

The sidewall angle was measured as 82° ± 3°, while sidewall roughness could not be quantified. SEM imaging required a conductive Electra 92 coating, reaching up to 40 nm on line tops and 200 nm in narrow gaps, which also covered the sidewalls and prevented reliable roughness extraction. Accurate evaluation would require low-voltage, high-resolution SEM without coating; alternatively, a thinner conductive layer (e.g., gold) may be used in future studies when more etched samples become available. Dips observed at the lower portions of the waveguide sidewalls can be minimized through further etch-recipe optimization.

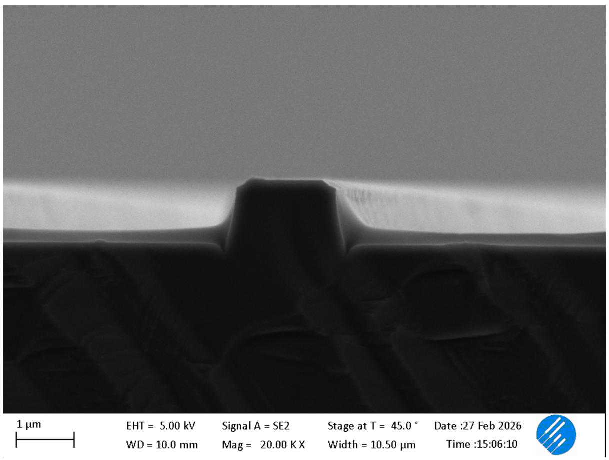

Figure 9: SEM image of a 2.1 μm 4H-SiC line linewidth and spacing of 5 μm

6. Future Work

In the continuation of this work, the measured sidewall angles and the refractive indices extracted from thin-film SiC can be incorporated into waveguide and bending analyses on the thin-film platform to tune target geometries. Once stable and reproducible lithography and etching results are consistently achieved, electron-beam lithography (EBL) trials can be initiated to further optimize the predefined waveguide dimensions. In parallel, ring-resonator analyses can be extended in greater detail.

References

[1] Tsunenobu Kimoto and James A. Cooper. *Fundamentals of Silicon Carbide Technology: Growth, Characterization, Devices, and Applications.* Wiley-IEEE Press, Singapore, 2014.

[2] M. A. Guidry, D. M. Lukin, K. Y. Yang, R. Trivedi, and J. Vučković. Quantum optics of soliton microcombs. *Nature Photonics*, 16(1):52–58, 2022.

[3] Miloš Popović. *Theory and Design of High-Index-Contrast Microphotonic Circuits.* Phd thesis, Massachusetts Institute of Technology, February 2008.

[4] S. Wang, M. Zhan, G. Wang, H. Xuan, W. Zhang, C. Liu, C. Xu, Y. Liu, Z. Wei, and X. Chen. 4h-sic: A new nonlinear material for midinfrared lasers. *Laser & Photonics Reviews*, 7:831–838, 2013.